Results in Physics 42 (2022) 106005

Contents lists available at ScienceDirect

Results in Physics

journal homepage: www.elsevier.com/locate/rinp

Mid-infrared chalcogenide slot waveguide plasmonic resonator sensor embedded with Au nanorods for surface-enhanced infrared absorption spectroscopy

Mingquan Pi [a,1], Huan Zhao [a,1], Chunguang Li [b,*], Yuting Min [a], Zihang Peng [a], Jialin Ji [a], Yijun Huang [a], Fang Song [a], Lei Liang [c], Yu Zhang [a], Yiding Wang [a], Frank K. Tittel [d], Chuantao Zheng [a,*]

[a] State Key Laboratory of Integrated Optoelectronics, College of Electronic Science and Engineering, Jilin University, 2699 Qianjin Street, Changchun 130012, China
[b] College of Biological and Agricultural Engineering, Jilin University, Changchun 130022, China
[c] State Key Laboratory of Luminescence and Applications, Changchun Institute of Optics Fine Mechanics and Physics, Chinese Academy of Sciences, Changchun 130033, China
[d] Department of Electrical and Computer Engineering, Rice University, 6100 Main Street, Houston, TX 77005, USA

ARTICLE INFO

Keywords:
Waveguide sensor
Slot waveguide
Nanorod
Surface-enhanced infrared absorption (SEIRA) spectroscopy

ABSTRACT

The problem of a traditional waveguide plasmonic resonator sensor is that part of the near-field intensity enhanced area is confined in the waveguide dielectric layer, which decreases the interaction effect between light and analyte. In order to solve this problem, a novel mid-infrared (MIR) chalcogenide (ChG) slot waveguide plasmonic resonator (SWGPR) sensor embedded with Au nanorods was proposed, where Au nanorods were used as antenna for enhancing mode coupling with the waveguide through resonance at the absorption wavelength of the analyte. The antenna parameters were optimized to make the resonance wavelength align with the absorption wavelength of the analyte. The proposed waveguide structure provides a sufficient sensing area and increases the electric field enhancement factor to > 6400. Polymethyl methacrylate (PMMA) and styrene were adopted as the analyte for sensing performance evaluation. The normalized absorption reaches 23.31 when the maximum extinction coefficient of PMMA is 0.08, which is at least 7 times higher than other silicon-on-insulator (SOI) waveguide plasmonic resonator sensors. The proposed waveguide structure provides a new idea for the design of other waveguide plasmonic resonator sensors with high sensing performance and has the potential for biochemical sensing.

Introduction

Fourier transform infrared (FTIR) spectrometer and other optical systems with discrete electrical/optical modules have been widely used for analyte measurement [1–8], but they are of large size and high cost. An on-chip optical waveguide sensor is miniature in size and shows superior performance using physical effects [9–13] or functional materials [14–16] to enhance sensitivity. Compared with the absorption in the near-infrared band, a majority of analytes has stronger absorption in the mid-infrared (MIR, 2.5–20 μm) band. Surface-enhanced infrared absorption (SEIRA) spectroscopy can be used for improving light field intensity and thus enhancing absorption. Therefore, using MIR waveguide and improving the light field intensity are the two solutions to increase sensitivity.

MIR silicon-on-insulator (SOI) rib waveguide plasmonic resonator sensor has been reported with a high enhancement factor of > 3600 in the optical field [17] for SEIRA sensing. However, silica (SiO_2) with a high loss in the MIR as lower buffer layer affects the sensing performance. Compared with SOI, chalcogenide (ChG) glass with a wide transparent window (1–20 μm) and a high refractive index (>2) is a kind of suitable material for fabricating low loss MIR optical waveguide [18]. Other MIR transparent materials (e.g. CaF_2 [19], sapphire [20–21]) can be used as the substrate of ChG waveguide. However, it is difficult for the light in the rectangular or rib waveguides to couple into antennas for

* Corresponding authors.
E-mail addresses: lichunguang@jlu.edu.cn (C. Li), zhengchuantao@jlu.edu.cn (C. Zheng).
[1] These two authors contribute equally to this work.

https://doi.org/10.1016/j.rinp.2022.106005
Received 26 May 2022; Received in revised form 16 September 2022; Accepted 18 September 2022
Available online 21 September 2022

SEIRA sensing and part of the near-field intensity enhanced area is confined in the waveguide dielectric layer, which cannot be adopted for sensing.

Waveguide plasmonic resonator sensor can strengthen the surface electric field to make the light-matter interaction more efficient [17,22–23], which is powerful for evanescent field sensing. Metal island structure can be used for SEIRA spectroscopy, but the enhancement factor is small and the fabrication cannot be repeatable [1]. An antenna can be a better alternative to metal island film. So far, different types of antennas, which can be integrated on optical waveguide, have been used for SEIRA spectroscopy (e.g. nanorod antenna [24–25], bowtie antenna [26–27], fan-shape antenna [28]). The size of an antenna influences the near-field intensity which can be improved by reducing the gap between antennas [29]. In 2018, Chen et al [17] demonstrated a rib waveguide sensor integrated with Au nanorods for SEIRA sensing. The gap between the nanorods was optimized to improve the sensing performance and the waveguide structure is shown in Fig. 1(a). In the same year, Mohr et al. [22] demonstrated waveguide sensors integrated with Au nanorods and Au nanoaperture for SEIRA sensing, as shown in Fig. 1(b) and (c), respectively. The major problem of these waveguide plasmonic resonator sensors is that the optical field enhancement factor and the normalized absorption are small, leading to a decrease in sensitivity.

To solve this problem, in this paper, a novel MIR ChG slot waveguide plasmonic resonator (SWGPR) sensor embedded with Au nanorods is demonstrated. The novel aspects of this sensor structure include: (1) Slot waveguide structure is used for improving the field intensity enhancement factor by making the slot overlap with the gap between the antennas, and the slot with a low refractive index provides enough sensing area for light-matter interaction. (2) Au nanorods are partially embedded in the waveguide and partially suspended in the slot, resulting in more suspended area for sensing operation. (3) The resonance wavelength of the sensor can be aligned with different absorption wavelength by changing the antenna width for the detection of any analytes. (4) The sensor length can be reduced by one or two orders by the use of the SWGPR sensing structure, which is helpful to the sensor miniaturization and high-density on-chip integration.

This paper is organized as follows. In Section 2, the structure of the SWGPR sensor and the sensing theory are presented. The structural parameters of the sensor are optimized and a feasible fabrication process is suggested. In Section 3, polymethyl methacrylate (PMMA) and styrene are used as the analyte for evaluating the sensing performance. The performances of the SWGPR sensor are compared with some reported rib and rectangular waveguide plasmonic resonator (RWGPR) sensor. The enhancement of the output absorption signal and the ability to reduce waveguide length are discussed for the SWGPR sensor. Some conclusions are reached in Section 4.

MIR ChG SWGPR sensor

Waveguide sensor structure

The 3D diagram of the MIR ChG SWGPR sensor is shown in Fig. 2(a). The sensor includes an input taper waveguide, a sensing area and an output taper waveguide. As_2Se_3 and CaF_2 are used as the waveguide core layer and substrate, respectively. The Au nanorods in the sensing area act as a resonator which are partially embedded in the waveguide and partially suspended in the slot. In this case, the slot with a low refractive index provides enough sensing area for light-matter interaction. Meanwhile, the Au nanorods are located in the middle of the waveguide core layer along the z direction, which improves the field intensity enhancement factor. Without sensing operation, air will be served as the cladding layer in the slot and other areas of the waveguide; whereas under sensing operation, the analyte will replace the air in the slot. A typical diagram of a measurement system based on such waveguide sensor is shown in Fig. 2(b). A broadband light source (e.g. optical parametric oscillators (OPO, M Squared, Firefly IR SW)) can be used as the light source. The light is coupled into and output from the waveguide through a fluoride optical fiber. A HgCdTe detector (e.g. Thorlabs, PDA10JT) can be used to probe the optical signal and the obtained electrical signal is sampled by a data acquisition (DAQ) card (e.g. National Instrument, USB-6211). A chopper (e.g. Thorlabs, MC1F10HP) and a lock-in amplifier (e.g. Stanford Research Systems, SR830) are used to suppress the $1/f$ noise through the modulation of the input light and the correlation demodulation of the output sensing signal. The cross-section structure of the slot waveguide with Au nanorods and the bare slot waveguide are shown in Fig. 2(c) and (d), respectively. The width and height of the waveguide core layer are defined as w_1 and h_1, respectively. The width of the slot is w_2. The structure of the Au antenna pairs is shown in Fig. 2(e). The structural parameters of the Au antenna include width w_3, length l_1, height h_2, gap width w_4 and distance l_2.

The refractive index of As_2Se_3 and CaF_2 are ~ 2.8 [31] and ~ 1.41 [30] at this wavelength range, respectively. The refractive index of air is set to 1. PMMA and styrene are adopted as the analyte for evaluating the sensing performance of the sensor. The refractive index of PMMA, styrene and Au can be obtained from the refractive index database [30]. Curves of the refractive index n and extinction coefficient κ of the PMMA versus wavelength are shown in Fig. 3(a). As can be seen that PMMA has a strong absorption near 3.4 μm and κ reaches the highest value at 3.39 μm, mainly due to the absorption of C — H [17]. Styrene has a strong absorption near 3.2 μm and κ becomes the maximum at 3.24 μm.

Waveguide sensing theory

The waveguide plasmonic resonator sensor obeys the temporal coupled mode theory. The Au nanorods and the analyte can be equivalent to two resonators. A principle diagram of the waveguide resonator

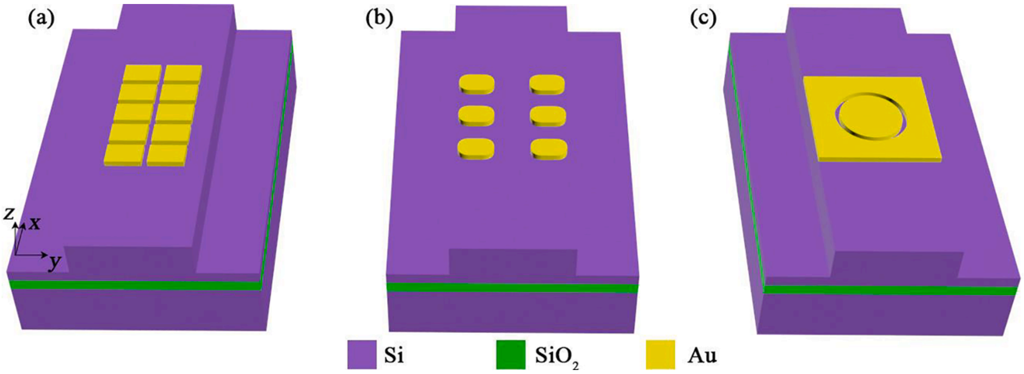

Fig. 1. The structure of rib waveguide sensor integrated with (a, b) Au nanorods, and (c) Au nanoaperture.

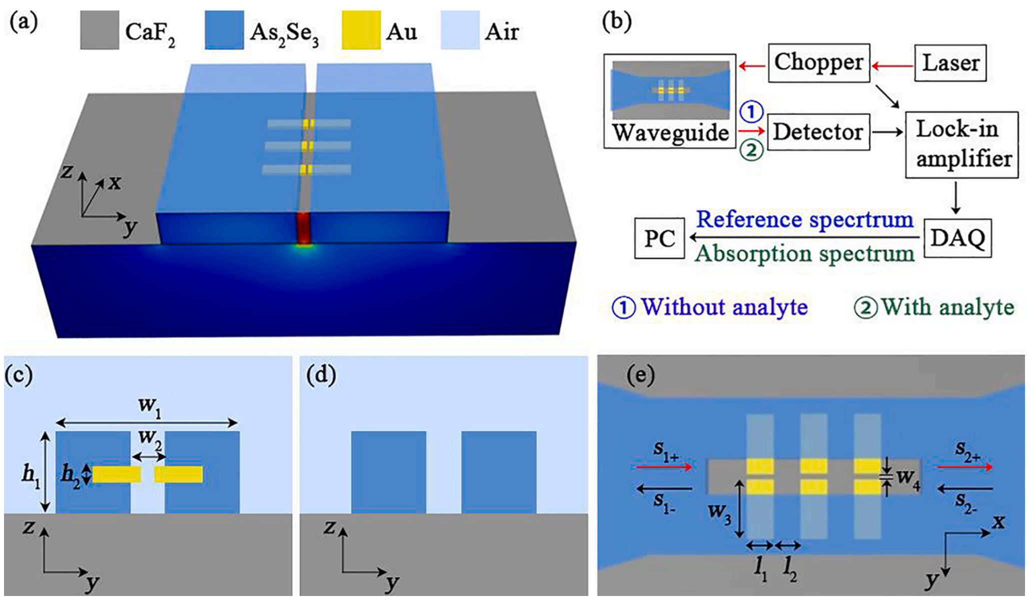

Fig. 2. (a) The 3D diagram of the MIR ChG SWGPR sensor. (b) The structure of a sensor system based on the SWGPR sensor. DAQ: data acquisition card; PC: personal computer. The cross-section structure of the (c) slot waveguide with Au nanorods and (d) bare slot waveguide. (e) The structure of the Au antenna pairs.

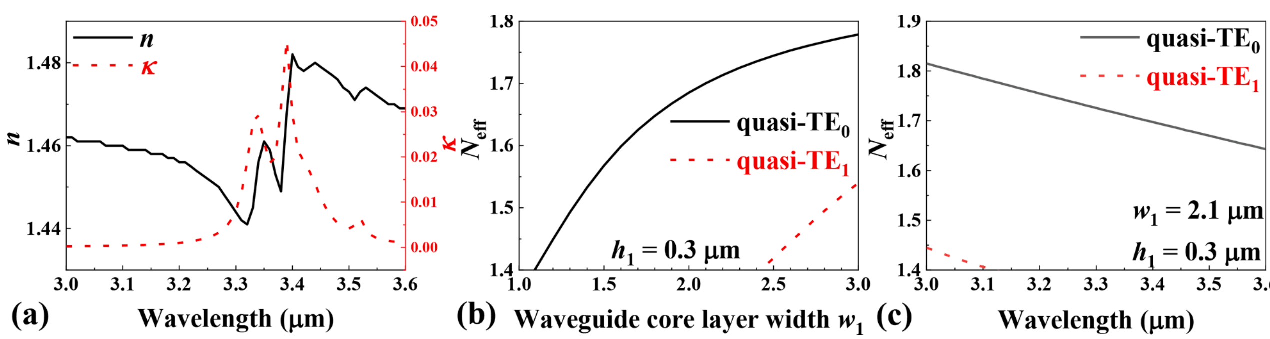

Fig. 3. (a) Curves of n and κ of PMMA versus wavelength. (b) Curves of the quasi-TE$_0$ mode and quasi-TE$_1$ mode effective refractive index N_{eff} of the rectangular waveguide versus core layer width w_1. (c) Curves of the quasi-TE$_0$ mode and quasi-TE$_1$ mode N_{eff} of the rectangular waveguide versus operation wavelength.

sensor is shown in Fig. 2(e). s_{1+} and s_{1-} are the amplitudes of the input modes, and s_{2+} and s_{2-} are the amplitude of the output modes. The following equations are used to express the relationship among these parameters [23]:

$$s_{1-} = C_{11}s_{1+} + a\kappa_{1a} + b\kappa_{1b} \tag{1}$$

$$s_{2-} = C_{21}s_{1+} + a\kappa_{2a} + b\kappa_{2b} \tag{2}$$

Here, a and b are the plasmonic resonance mode amplitude and the analyte absorbance resonance amplitude, respectively; C_{ij} is the coupling constant between s_{i-} and s_{j+} ($i, j = 1, 2$); κ_{ia} and κ_{ib} are the coupling coefficients between s_{i+} and a, b, respectively. The transfer function of the waveguide can be expressed as.

$$T = \left|\frac{s_{2-}}{s_{1+}}\right|^2 \tag{3}$$

The transmission spectrum of the waveguide with analyte can be defined as the absorption spectrum (the extinction coefficient $\kappa \neq 0$) and the reference spectrum ($\kappa = 0$) [17].

When the input light resonates with the antenna, the electric field in the gap between the antenna pairs will be greatly enhanced, which will strengthen the absorption of analyte. The enhancement factor of the field intensity $|E/E_0|^2$ can be used to evaluate the resonance effect between light and antenna, where E and E_0 are the electric field amplitude along the mode propagation direction and the input electric field amplitude, respectively. After spinning an analyte to the surface of the Au nanorods, the increased absorption loss will influence the mode coupling between Au nanorods and the waveguide. The normalized absorption (NA) is defined as [22].

$$\mathrm{NA} = \frac{T_a(\lambda) - T_r(\lambda)}{T_r(\lambda)} \tag{4}$$

Here, $T_a(\lambda)$ and $T_r(\lambda)$ are the transmittances of the absorption spectrum and reference spectrum at λ. NA indicates the effect of the enhanced absorption of the analyte on the coupling efficiency of the antenna, which can indirectly characterize the influence of the antenna on the enhancement of absorption.

Waveguide sensor optimization

Simulation method

COMSOL Multiphysics was used to optimize the structure of the ChG SWGPR sensor and to analyse the sensing performances. The structural parameters and material parameters of the waveguide were set. The Electromagnetic Waves, Frequency Domain interface of the Wave Optics branch was used to obtain electric field distributions. All the optimization results are based on the parametric sweep module in COMSOL.

The frequency domain was used in the Study branch for calculating transmission spectrum of the sensor. Input port and output port were added at the waveguide input interface and waveguide output interface to generate excitation at a specific frequency. The performance of the sensor at each wavelength can be obtained and optimized by parametric sweep. The electric field distribution and transmission spectrum can be obtained at Results branch. The wavelength and frequency of light can be transformed into each other, so the results based on wavelength can be obtained by frequency domain analysis. The excitation of the device in the frequency domain and the wavelength domain is similar, because the software calculates the response of the device when using frequency and wavelength excitation, respectively. We simulated the sensor in the frequency domain with reference to the accurate methods in other theoretical calculation work [22].

Different from the simulation of the transmission spectrum of the sensor, the mode analysis is added to the Study branch with a specific frequency for excitation instead of the frequency domain to obtain effective refractive index N_{eff}. Because the mode analysis is aimed at the waveguide cross-section structure, there is no need to add the input port and output port. The N_{eff} and electric field distribution of the waveguide mode can be obtained at Results branch.

Single-mode waveguide design

The structure of rectangular waveguide is optimized to satisfy the single mode condition. The quasi-TE$_0$ mode is used for producing horizontal resonance and to improve the field intensity in the gap. Curves of the quasi-TE$_0$ mode and quasi-TE$_1$ mode N_{eff} of the rectangular waveguide versus core layer width w_1 are shown in Fig. 3(b), where $h_1 = 0.3$ μm and the wavelength is 3.39 μm. N_{eff} increases with the increase of w_1 and the single mode condition is satisfied when $w_1 \leq 2.4$ μm. w_1 cannot be too small because the transition from rectangular waveguide to slot waveguide reduces N_{eff} [31–32] and the slot waveguide should satisfy the condition of guiding light. So w_1 and h_1 are set to be 2.1 μm and 0.3 μm, respectively. Curves of the N_{eff} of the optimized rectangular waveguide versus the operation wavelength are shown in Fig. 3(c). The single mode condition is satisfied in the wavelength range from 3.2 μm to 3.6 μm, which covers the absorption peak of PMMA. The electric field distribution of the quasi-TE$_0$ mode of the rectangular waveguide at 3.39 μm is shown in Fig. 4(a). Along the direction of optical transmission, the cross-section structure of the waveguide will become a slot waveguide, whose electric field distribution of the quasi-TE$_0$ mode at 3.39 μm is shown in Fig. 4(b).

Antenna optimization

The antenna structure is optimized to make the resonance wavelength align with the absorption peak of the analyte and to improve the field intensity enhancement factor [23]. In order to obtain sufficient sensing area and ensure the interaction between the two strips of the slot waveguide, w_2 is set to 100 nm. Reducing w_4 can increase the electric field intensity in the gap [29]. Considering the fabrication feasibility, w_4 is set to 20 nm and h_2 is 30 nm. The transmission spectrum for different w_3 from 300 nm to 345 nm and the curve of the resonance wavelength versus w_3 are shown in Fig. 5(a) and Fig. 5(b), respectively, where $l_1 = 100$ nm, $l_2 = 210$ nm and $\kappa = 0$. The transmission spectrum for different l_1 from 80 nm to 100 nm are shown in Fig. 5(c), where $w_3 = 335$ nm, $l_2 = 210$ nm and $\kappa = 0$. The transmission spectrum has a red shift with the increase of w_3 or decrease of l_1. The resonance wavelength is aligned with the PMMA absorption wavelength when $w_3 = 335$ nm and $l_1 = 100$ nm. The transmission spectrum of the sensor under different l_2 from 190 nm to 230 nm are shown in Fig. 5(d), where $w_3 = 335$ nm, $l_1 = 100$ nm

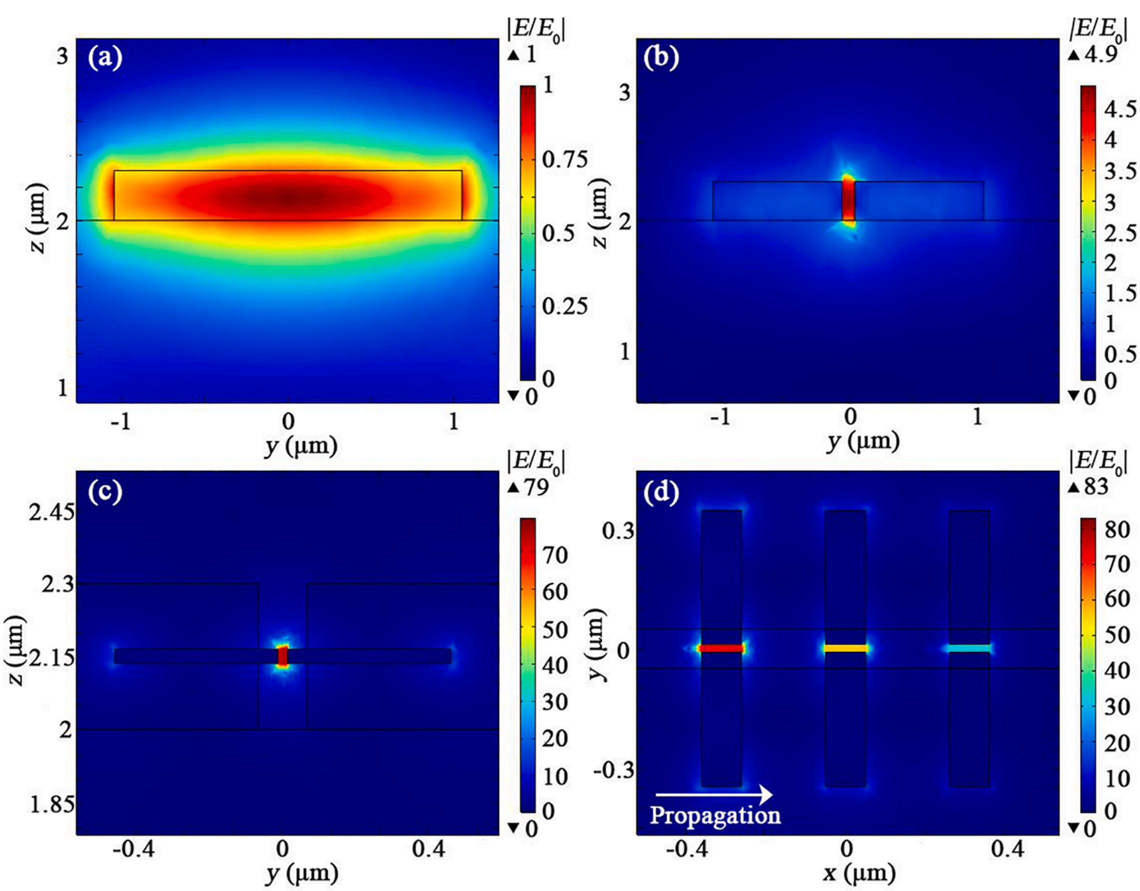

Fig. 4. (a) The electric field distribution of the quasi-TE$_0$ mode of the rectangular waveguide at 3.39 μm. (b) The electric field distribution of the quasi-TE$_0$ mode of the slot waveguide at 3.39 μm. (c) The electric field distribution in the *yz* plane at the center of the first antenna pair in the *x* direction. (d) The electric field distribution in the *xy* plane at the center of the antenna pairs in the *z* direction.

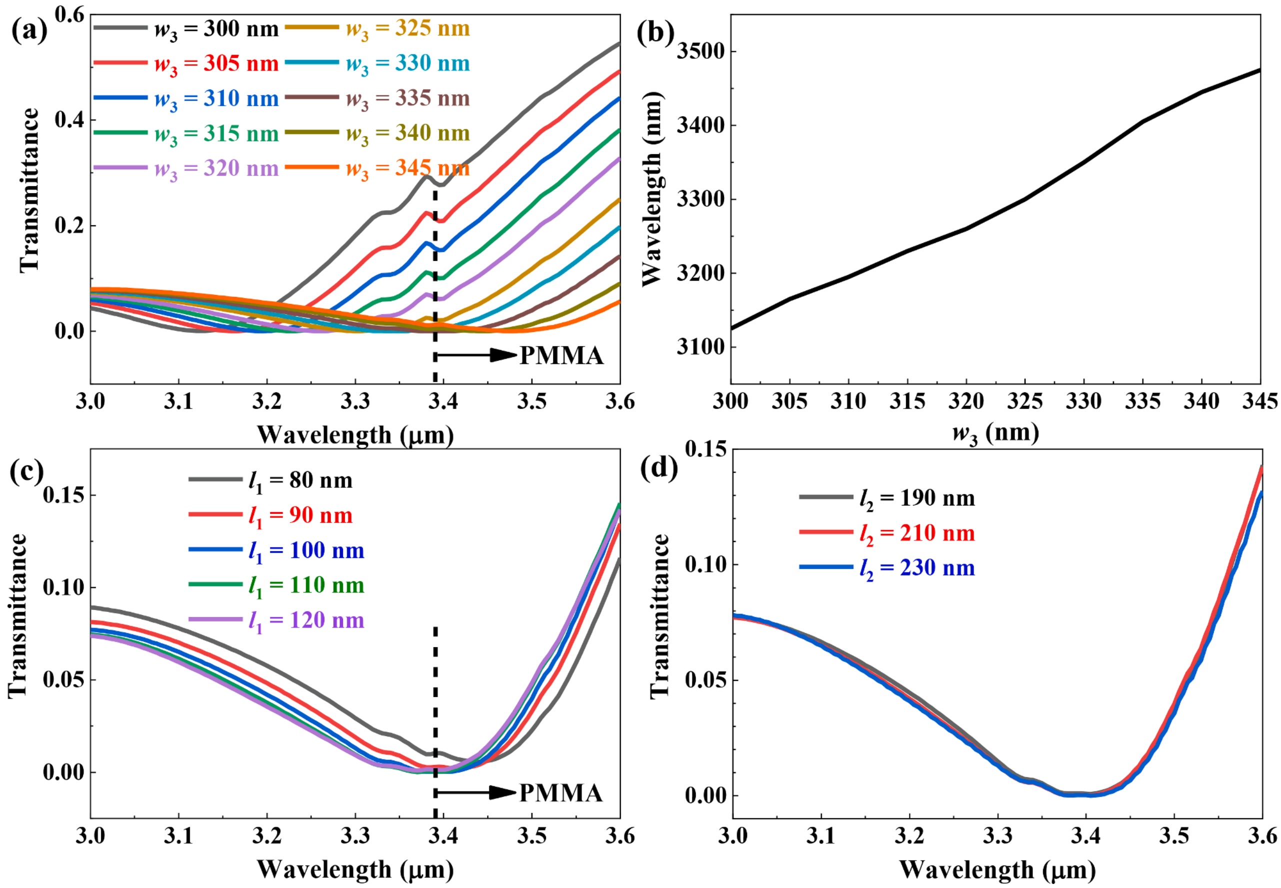

Fig. 5. (a) Transmission spectrum of the SWGPR sensor at different w_3 from 300 nm to 345 nm, where $l_1 = 100$ nm, $l_2 = 210$ nm and $\kappa = 0$. (b) Curve of the resonance wavelength of the SWGPR sensor versus w_3, where $l_1 = 100$ nm, $l_2 = 210$ nm and $\kappa = 0$. (c) Transmission spectrum of the SWGPR sensor at different l_1 from 80 nm to 100 nm, where $w_3 = 335$ nm, $l_2 = 210$ nm and $\kappa = 0$. (d) Transmission spectrum of the SWGPR sensor at different l_2 from 190 nm to 230 nm, where $w_3 = 335$ nm, $l_1 = 100$ nm and $\kappa = 0$.

and $\kappa = 0$. The transmission spectrum hardly shifts with l_2, which is set to 210 nm in the design. Therefore, the variation of l_2 on the resonance wavelength can be ignored, and the resonance peak and the absorption peak can be aligned by adjusting w_3 and l_1. So the optimization results of antenna are $w_3 = 335$ nm and $l_1 = 100$ nm and $l_2 = 210$ nm. The final optimized ChG SWGPR sensor parameters are listed in Table 1. The electric field distribution in the *yz* plane at the center of the first antenna pair in the *x* direction is shown in Fig. 4(c). The electric field distribution in the *xy* plane at the center of the antenna pairs in the *z* direction is shown in Fig. 4(d). The area where the significantly enhanced electric field intensity is concentrated near the gap and the enhancement factor $|E/E_0|$ reaches 83. Sufficient sensing area and enhanced electric intensity ensure a good sensing performance.

Table 1
The optimized parameters of the ChG SWGPR sensor.

Sensor structural parameters	Value
Waveguide core layer width, w_1	2.1 μm
Slot width, w_2	100 nm
Antenna width, w_3	335 nm (for PMMA) 318 nm (for styrene)
Gap width, w_4	20 nm
Waveguide core layer height, h_1	0.3 μm
Antenna height, h_2	30 nm
Antenna length, l_1	100 nm
Antenna distance, l_2	210 nm

Fabrication process

The suggested fabrication process of the sensing area for the SWGPR sensor is shown in Fig. 6, which can be used for future experimental verification. First, As_2Se_3 rectangular waveguide is fabricated on CaF_2 substrate by lift-off method (Fig. 6(a)). The input taper waveguide and the output taper waveguide are also fabricated in this step. Then the thickness of the rectangular waveguide in the sensing area is reduced by lithography and inductively coupled plasma (ICP) etching (Fig. 6(b)). Next, the slot structure is obtained by electron beam lithography (EBL) and ICP etching (Fig. 6(c)). Under the protection of a photoresist mask, SiO_2 is deposited into the slot by chemical vapor deposition (CVD) (Fig. 6(d)). Then Au nanorods are fabricated by another lift-off processing (Fig. 6(e)). Next, SiO_2 is deposited into the gap also by CVD under the protection of the photoresist mask (Fig. 6(f)). Then As_2Se_3 previously removed by etching (Fig. 6(b)) is fabricated again by lift-off method (Fig. 6(g)). The slot at the top of the waveguide is obtained by EBL and ICP etching (Fig. 6(h)). Finally, SiO_2 is removed by HF etching (Fig. 6(i)).

Waveguide sensing performance

In this Section, PMMA and styrene are adopted as two analytes for the performance evaluation of the waveguide sensor. A key figure of merit is to observe the enhancement factor in terms of infrared absorption due to the use of the waveguide resonator structure.

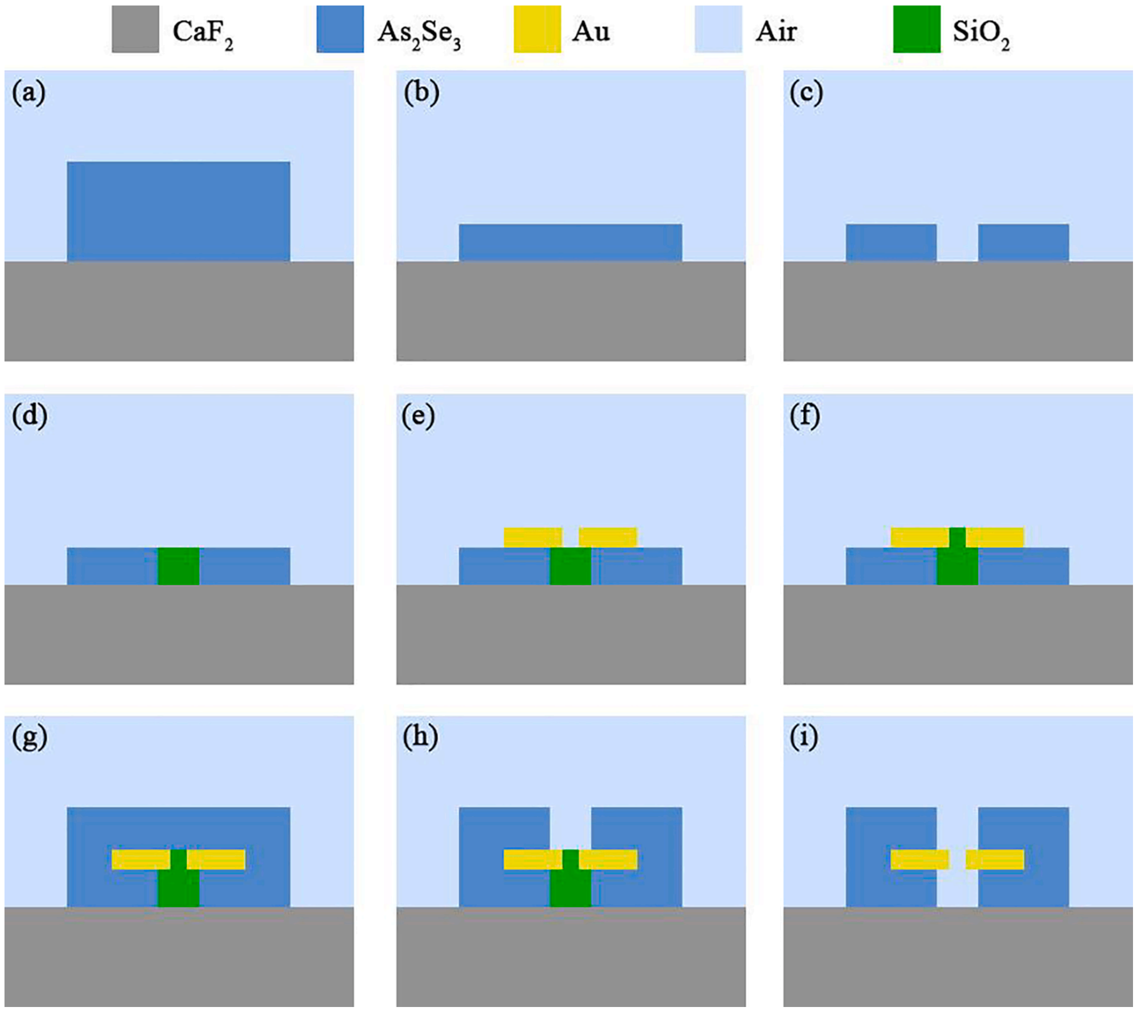

Fig. 6. Waveguide fabrication process in the sensing region for the MIR ChG SWGPR sensor. (a) As_2Se_3 rectangular waveguide fabrication on CaF_2 substrate by lift-off method. (b) Lithography and ICP etching of the rectangular waveguide. (c) EBL and ICP etching of the lower slot. (d) SiO_2 deposition into the slot by CVD. (e) Au nanorods fabrication by lift-off method. (f) SiO_2 deposition into the gap by CVD. (g) As_2Se_3 fabrication by lift-off method. (h) EBL and ICP etching of the upper slot. (i) SiO_2 removal by HF etching.

SEIRA sensing based on ChG SWGPR sensor

Take PMMA as analyte. During sensing operation of the ChG SWGPR sensor, PMMA is required to wrap around each Au antenna pair. The width, height and length of the PMMA area are 100 nm, 120 nm and 180 nm, respectively. The cross-section structure of the Au antenna pair is shown in the inset of Fig. 7(a). The reference spectrum and absorption spectrum of the ChG SWGPR sensor are shown in Fig. 7(a). The transmission is greatly reduced at the wavelength of 3.39 μm due to absorption. Curve of |NA| versus the operation wavelength is shown in Fig. 7(d). It can be seen that |NA| reaches the maximum value of 15.37 at 3.39 μm.

Then, the PMMA under the nanorods is removed to simulate the situation that the waveguide dielectric layer occupies the sensing area. The cross-section structure in the *yz* plane of the Au antenna pair wrapped in partial PMMA is shown in the inset of Fig. 7(b). The reference spectrum and absorption spectrum are shown in Fig. 7(b). Curve of |NA| versus wavelength is shown in Fig. 7(d). In this case, NA only reaches 10.43 at 3.39 μm. Therefore, |NA| can be increased by ~ 50 % when the sensing area at the bottom of the Au antenna pair is utilized for sensing.

The resonance wavelength of the sensor can be changed with the variation of w_3 (Fig. 5(b)). In order to illustrate the advantage of the ChG SWGPR sensor structure, another analyte, styrene is used to evaluate the sensing performance, which is listed as a kind of class 2B carcinogens by the World Health Organization's International Agency for Research on Cancer. Curves of n and κ of styrene versus wavelength are shown in Fig. 8(a). w_3 is set to 318 nm to make the resonance wavelength align with the absorption peak wavelength of styrene at 3245 nm. The width, height and length of the sensing area filled with styrene are 100, 34 and 104 nm, considering the thickness of the self-assembled monolayer liquid molecule of ~ 2 nm [22]. The reference spectrum, absorption spectrum and NA of styrene are shown in Fig. 8(b), respectively. The obtained NA at the absorption peak is 3.32, which is smaller than that of PMMA because of a lower κ of 0.018.

SEIRA sensing based on ChG RWGPR sensor

In order to further show the effect of the bottom area of the Au antenna pairs on sensing performance, we investigate the ChG RWGPR sensor whose 3D diagram is shown in the inset of Fig. 7(c). The width and height of the rectangular waveguide are the same as the slot waveguide sensor. The width of the antenna is changed to 380 nm to make the resonance wavelength aligned with the PMMA absorption wavelength. The height of the PMMA analyte is reduced to 75 nm, and the cross-section structure in the *yz* plane of the Au antenna pair wrapped in PMMA is shown in the inset of Fig. 7(c). The reference spectrum and absorption spectrum are shown in Fig. 7(c). It can be

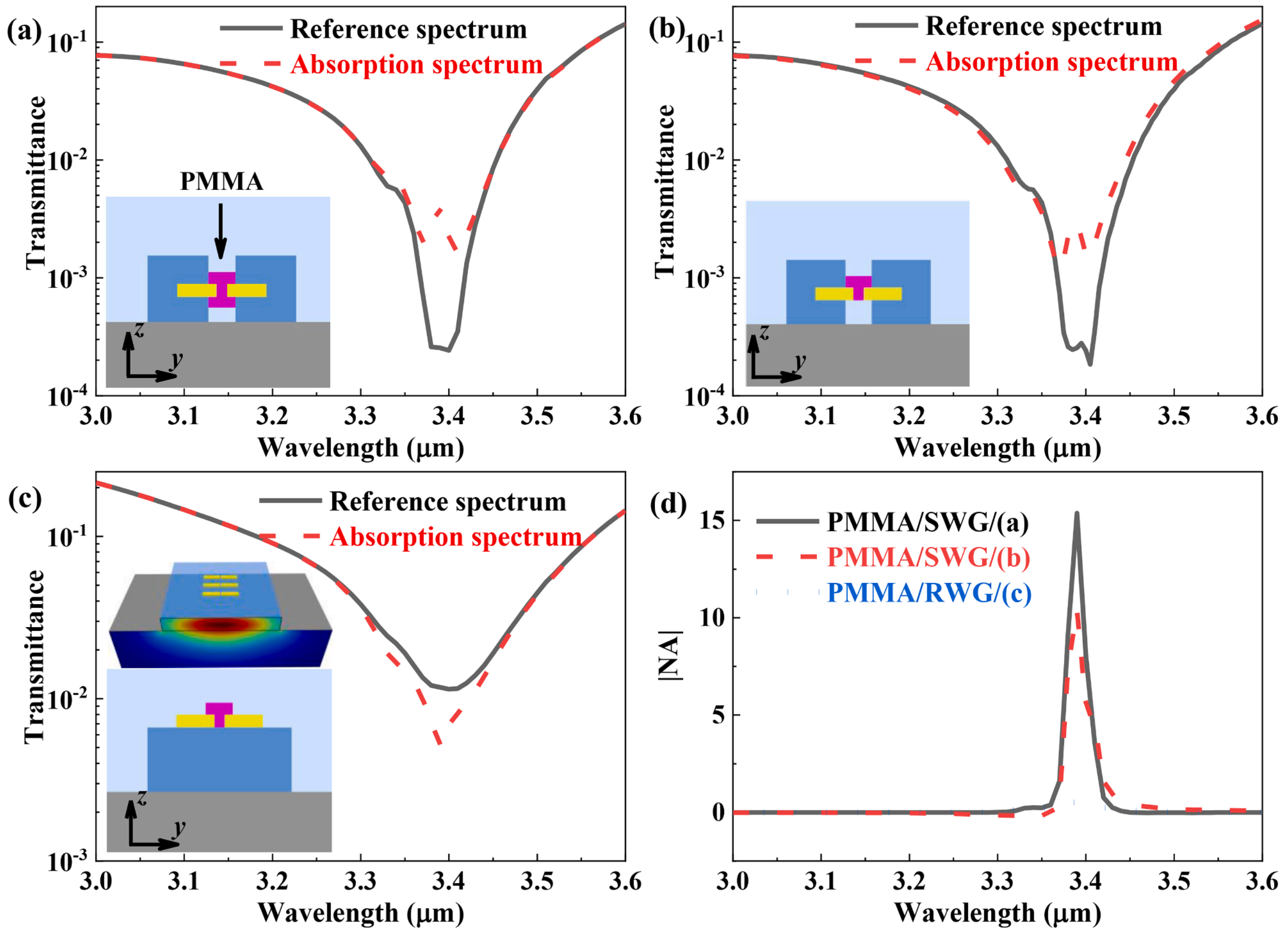

Fig. 7. (a) The reference spectrum and absorption spectrum of the ChG SWGPR sensor when the Au antenna pairs are wrapped in PMMA. Inset: the cross-section structure in the *yz* plane of the Au antenna pairs wrapped in PMMA. (b) The reference spectrum and absorption spectrum of the ChG SWGPR sensor when the Au antenna pairs are wrapped in partial PMMA. Inset: the cross-section structure in the *yz* plane of Au antenna pairs wrapped in partial PMMA. (c) The reference spectrum and absorption spectrum of the ChG RWGPR sensor. Inset: the 3D diagram of the sensor and the cross-section structure in the *yz* plane of Au antenna pairs wrapped in PMMA. (d) Curves of |NA| of the ChG SWGPR sensor versus wavelength when the Au antenna pairs wrapped in PMMA and partial PMMA, and the |NA| of the ChG RWGPR sensor versus wavelength when the Au antenna pairs wrapped in PMMA.

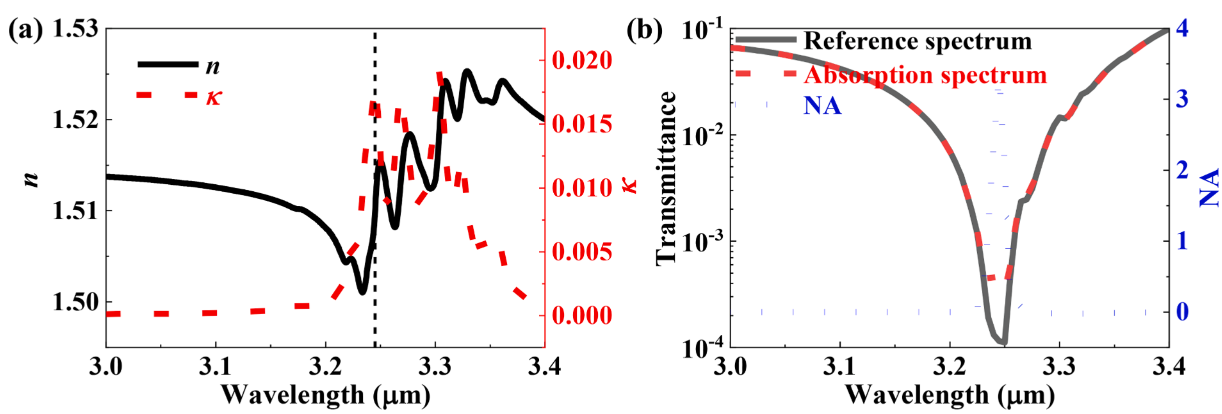

Fig. 8. (a) Curves of n and κ of styrene versus wavelength. (b) The reference spectrum, absorption spectrum and NA of styrene using the SWGPR sensor.

found that $T_a(\lambda)$ is smaller than that of the $T_r(\lambda)$, resulting in a negative NA. Curve of |NA| for the ChG RWGPR sensor versus the operation wavelength is shown in Fig. 7(d). The obtained |NA| is < 1, because the bottom area of the Au antenna pair is filled with As_2Se_3, and PMMA has less effect on the light coupled into the antennas, which weakens the effect of the Au nanorods on PMMA.

Absorption enhancement

As a clear evidence of the sensor for absorption enhancement, the performances of some other reported waveguide plasmonic resonator sensors using PMMA as analyte with the same absorption wavelength range are compared with those of the proposed ChG SWGPR sensor, as shown in Table 2. The maximum κ of PMMA in other reports is > 0.08,

Table 2
Comparison among the proposed ChG SWGPR sensor and other reported waveguide sensors.

Refs.	Waveguide material	Waveguide type	Antenna type	$\|E/E_0\|$	NA
23	SOI	Rib	Nanorod	40	3.3 ($\kappa > 0.08$)
22	SOI	Rib	Nanorod	15	0.02 ($\kappa > 0.08$)
22	SOI	Rib	Nanoaperture	33	0.07 ($\kappa > 0.08$)
This paper	ChG	Rectangular	Nanorod	52.7	−0.56 ($\kappa = 0.046$)
This paper	ChG	Slot	Nanorod	83	15.37 ($\kappa = 0.046$) 23.31 ($\kappa = 0.08$)

which is larger than the maximum κ ($\kappa = 0.046$) in this paper. In order to make the comparison more reasonable, $\kappa = 0.08$ is also taken into account in this comparison. The NA of the ChG SWGPR sensor rises to 23.31 when $\kappa = 0.08$. Compared to other SOI rib waveguide sensors, the ChG SWGPR sensor has the largest $|E/E_0|$ and NA, and NA is at least 7 times higher than other SOI rib waveguide sensors. Therefore, the presented waveguide sensor structure will be beneficial to increase measurement sensitivity due to a large signal variation.

Sensing length reduction and miniaturization

A traditional waveguide sensor based on evanescent field absorption (Fig. 9(c)) and a sensor based on bulk material absorption (Fig. 9(b)) can be used for absorption measurement of an analyte, which generally obeys the Lambert-Beer law. For a dielectric waveguide, power confinement factor (PCF) in the sensing area determines the absorption of the analyte [31]. The PCF of an evanescent field based waveguide sensor is generally < 1 and the PCF of a sensor using bulk material absorption is equal to 1. Therefore, for achieving the same absorbance, a traditional waveguide sensor simply based on evanescent field absorption will have a longer length. Compared to the sensing scheme simply based on bulk material absorption (i.e. light propagates through the analyte) and the scheme based on evanescent field absorption, in order to illustrate the advantage of the SWGPR sensor (Fig. 9(a)) in waveguide length reduction, the effective sensing lengths for achieving the same absorbance of the proposed sensor are compared for the three schemes. Curves of sensor length versus absorbance are shown in Fig. 9(d) and the comparison results are shown in Table 3. The absorbance of the proposed sensor with an effective sensing length of L_1 is 1 μm. The effective path length based on bulk material absorption L_2 (=21.52 μm) is > 21 times larger than L_1 to achieve the same absorbance as this sensor. For the evanescent field based waveguide sensor, the effective sensing length is equal to L_2/PCF. Normally, the PCF of a bare slot waveguide sensor is 30 %, so L_3 (=L_2/30 % = 71.73 μm) is > 70 times larger than L_1.

Table 3
Comparison of the sensor length with the same absorbance for the three schemes.

Sensing scheme	Sensor type	Length (μm)
SEIRA	SWGPR	1
Bulk material absorption	Bulk PMMA	21.52
Evanescent field absorption	Bare slot waveguide	71.73
	Bare rectangular waveguide	> 107.60

For example, a bare rectangular waveguide is widely used for evanescent field sensing with a PCF of < 20 %, so L_1 can be reduced at least 100 times (>L_2/20 % = 107.60) than the bare rectangular waveguide. Therefore, the proposed SWGPR is of great significance to sensor miniaturization. Microring resonator can also reduce the device length with large interaction length through resonance, but the ring waveguide occupies a large area and the resonance wavelength is difficult to align with the absorption peak considering unavoidable fabrication errors [32].

Conclusions

A novel MIR ChG SWGPR sensor was proposed for SEIRA sensing. PMMA and styrene were adopted as the analytes for sensing performance evaluation. The antenna parameters were optimized to make the resonance wavelength align with the absorption wavelength of the two analytes. The novel ChG slot waveguide structure increased the electric field enhancement factor and provided a sufficiently large sensing area. The $|E/E_0|$ and NA reach 83 and 23.31 when the maximum κ of PMMA is 0.08, which is at least 7 times larger than other SOI waveguide plasmonic resonator sensors. The proposed sensor reduced the device length by at least two orders of magnitude than other evanescent field based rectangular waveguide sensors, which is of great significance to the miniaturization of the device. The resonance wavelength can be aligned

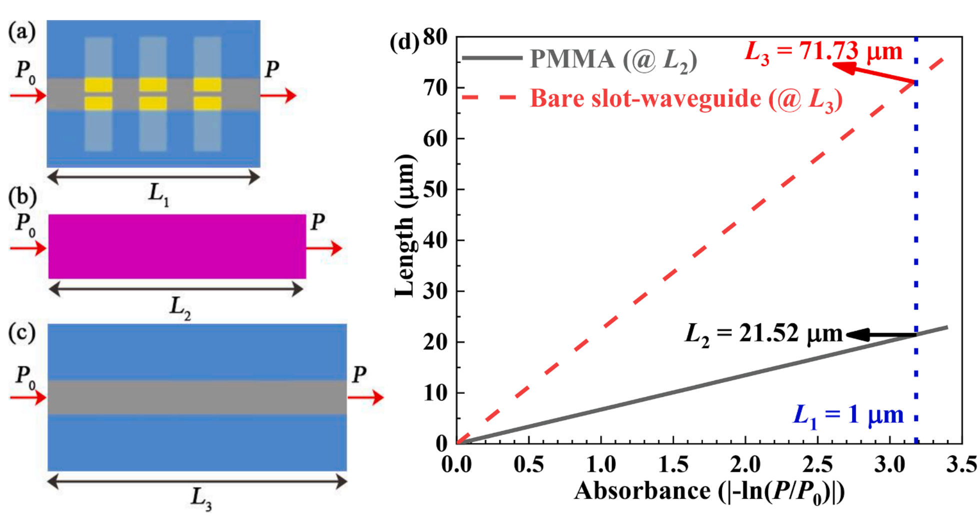

Fig. 9. The schematic diagrams of the (a) SWGPR sensor with a length of L_1 = 1 μm, (b) the bare PMMA with a length of L_2, and (c) the bare slot waveguide sensor with a length of L_3. P: the output power. P_0: the input power. (d) Curves of the sensor length (L_2, L_3) versus the absorbance.

with different absorption wavelength by changing the antenna width for the detection of different analytes. The styrene measurement shows that the proposed sensor has the potential for biochemical sensing.

CRediT authorship contribution statement

Mingquan Pi: Conceptualization, Methodology, Investigation, Writing – original draft. **Huan Zhao:** Investigation, Validation, Writing – review & editing. **Chunguang Li:** Investigation, Writing – review & editing, Funding acquisition. **Yuting Min:** Investigation, Validation. **Zihang Peng:** Investigation, Validation. **Jialin Ji:** Investigation. **Yijun Huang:** Investigation. **Fang Song:** Writing – review & editing. **Lei Liang:** Writing – review & editing. **Yu Zhang:** Writing – review & editing. **Yiding Wang:** Resources, Funding acquisition. **Frank K. Tittel:** Writing – review & editing. **Chuantao Zheng:** Conceptualization, Investigation, Writing – review & editing, Funding acquisition.

Declaration of Competing Interest

The authors declare that they have no known competing financial interests or personal relationships that could have appeared to influence the work reported in this paper.

Data availability

Data will be made available on request.

Acknowledgements

The authors wish to express their gratitude to the National Natural Science Foundation of China (Nos. 62175087, 61960206004), Key Science and Technology R&D program of Jilin Province, China (No. 20200401059GX, 20200201228JC), Science and Technology Research Project of Department of Education, Jilin Province, China (No. JJKH20211088KJ), Program for JLU Science and Technology Innovative Research Team (JLUSTIRT, 2021TD-39).

References

[1] Cheruvalath A, Nampoori VPN, Thomas S. Oblique angle deposited silver islands on $Ge_{20}Se_{70}Te_{10}$ film substrate for surface-enhanced infrared spectroscopy. Sens Actuators B: Chem 2019;287:225–30.
[2] Verge F, Paina T, Nazabal V, Boussard-Pledel C, Bureaua B, Colas F, et al. Surface enhanced infrared absorption (SEIRA) spectroscopy using gold nanoparticles on As_2S_3 glass. Sens Actuators B: Chem 2012;175:142–8.
[3] Yoo D, Mohr DA, Vidal-Codina F, John-Herpin A, Jo M, Kim S, et al. High-contrast infrared absorption spectroscopy via mass-produced coaxial zero-mode resonators with sub-10 nm Gaps. Nano Lett 2018;18:1930–6.
[4] Zheng C, Ye W, Sanchez NP, Li C, Dong L, Wang Y, et al. Development and field deployment of a mid-infrared methane sensor without pressure control using interband cascade laser absorption spectroscopy. Sens Actuators B: Chem 2017; 244:365–72.
[5] Li B, Zheng C, Liu H, He Q, Ye W, Zhang Y, et al. Development and measurement of a near-infrared CH_4 detection system using 1.654 μm wavelength-modulated diode laser and open reflective gas sensing probe. Sens Actuators B: Chem 2016;225: 188–98.
[6] Dong M, Zheng C, Yao D, Zhong G, Miao S, Ye W, et al. Double-range near-infrared acetylene detection using a dual spot-ring Herriott cell (DSR-HC). Opt Express 2018;26:12081–91.
[7] Song F, Zheng C, Yan W, Ye W, Wang Y, Tittel FK. Interband cascade laser based mid-infrared methane sensor system using a novel electrical-domain self-adaptive direct laser absorption spectroscopy (SA-DLAS). Opt Express 2017;25:31876–88.
[8] He Q, Zheng C, Lou M, Ye W, Wang Y, Tittel FK. Dual-feedback mid-infrared cavity-enhanced absorption spectroscopy for H_2CO detection using a radio-frequency electrically-modulated interband cascade laser. Opt Express 2018;26:15436–44.
[9] Qi Y, Yang F, Lin Y, Jin W, Ho HL. Nanowaveguide enhanced photothermal interferometry spectroscopy. J Lightwave Technol 2017;35:5267–75.
[10] Kraeh C, Martinez-Hurtado JL, Popescu A, Hedler H, Finley JJ. Slow light enhanced gas sensing in photonic crystals. Opt Mater 2018;76:106–10.
[11] Peyskens F, Dhakal A, Dorpe PV, Thomas NL, Baets R. Surface Enhanced raman spectroscopy using a single mode nanophotonic-plasmonic platform. ACS Photon 2016;3:102–8.
[12] Chamanzar M, Adibi A. Hybrid nanoplasmonic-photonic resonators for efficient coupling of light to single plasmonic nanoresonators. Opt Express 2011;19: 22292–304.
[13] Chamanzar M, Xia Z, Yegnanarayanan S, Adibi A. Hybrid integrated plasmonic-photonic waveguides for on-chip localized surface plasmon resonance (LSPR) sensing and spectroscopy. Opt Express 2013;21:32086–98.
[14] Wang GQ, Wang CN, Sun SQ. An optical waveguide sensor based on mesoporous silica films with a comparison to surface plasmon resonance sensors. Sens Actuators B: Chem 2018;255:3400–8.
[15] Gutierrez-Arroyo A, Baudet E, Bodiou L, Nazabal V, Rinnert E, Michel K, et al. Theoretical study of an evanescent optical integrated sensor for multipurpose detection of gases and liquids in the Mid-Infrared. Sens Actuators B: Chem 2017; 242:842–8.
[16] Gao L, Yang X, Shu Y, Chen X, Wang J. Ionic liquid-based slab optical waveguide sensor for the detection of ammonia in human breath. J Colloid Interf Sci 2018; 512:819–25.
[17] Chen C, Mohr DA, Choi H, Yoo D, Li M, Oh S. Waveguide-Integrated Compact Plasmonic Resonators for On-Chip Mid-Infrared Laser Spectroscopy. Nano Lett 2018;18:7601–8.
[18] Viens JF, Meneghini C, Villeneuve A, Galstian TV, Knystautas EJ, Duguay MA, et al. Fabrication and characterization of integrated optical waveguides in sulfide chalcogenide glasses. J Lightwave Technol 1999;17:1184–91.
[19] Chen Y, Lin H, Hu J, Li M. Heterogeneously Integrated Silicon Photonics for the Mid-Infrared and Spectroscopic Sensing. ACS Nano 2014;8:6955–61.
[20] Shankar R, Bulu I, Loncar M. Integrated high-quality factor silicon-on-sapphire ring resonators for the mid-infrared. Appl Phys Lett 2013;102:051108.
[21] Smith CJ, Shankar R, Laderer M, Frish MB, Loncar M, Allen MG. Sensing nitrous oxide with QCL-coupled silicon-on-sapphire ring resonators. Opt Express 2015;23: 5491–9.
[22] Mohr DA, Yoo D, Chen C, Li M, Oh S. Waveguide-integrated mid-infrared plasmonics with high-efficiency coupling for ultracompact surface-enhanced infrared absorption spectroscopy. Opt Express 2018;26:23540–9.
[23] Chen C, Oh S, Li M. Coupled-mode theory for plasmonic resonators integrated with silicon waveguides towards mid-infrared spectroscopic sensing. Opt Express 2020; 28:2020–36.
[24] Neubrech F, Weber D, Katzmann J, Huck C, Toma A, Fabrizio ED, et al. Infrared optical properties of nanoantenna dimers with photochemically narrowed gaps in the 5 nm regime. ACS Nano 2012;6:7326–32.
[25] Rodrigo D, Tittl A, John-Herpin A, Limaj O, Altug H. Self-similar multiresonant nanoantenna arrays for sensing from near- to mid-infrared. ACS Photon 2018;5: 4903–11.
[26] Navarro-Cia M, Maier SA. Broad-band near-infrared plasmonic nanoantennas for higher harmonic generation. ACS Nano 2012;6:3537–44.
[27] Dong L, Yang X, Zhang C, Cerjan B, Zhou L, M.L. T, Y. Zhang, A. Alabastri, P. Nordlander, and N.J. Halas,. Nanogapped Au Antennas for Ultrasensitive Surface-Enhanced Infrared Absorption Spectroscopy. Nano Lett 2017;17:5768–74.
[28] Brown LV, Yang X, Zhao K, Zheng BY, Nordlander P, Halas NJ. Fan-Shaped Gold Nanoantennas above Reflective Substrates for Surface-Enhanced Infrared Absorption (SEIRA). Nano Lett 2015;15:1272–80.
[29] Dong B, Ma Y, Ren Z, Lee C. Recent progress in nanoplasmonics-based integrated optical micro/nano-systems. J Phys D: Appl Phys 2020;53:213001.
[30] https://refractiveindex.info/.
[31] Pi M, Zheng C, Bi R, Zhao H, Liang L, Zhang Y, et al. Design of a mid-infrared suspended chalcogenide/silica-on-silicon slot waveguide spectroscopic gas sensor with enhanced light-gas interaction effect. Sens Actuators B: Chem 2019;297: 126732.
[32] Pi M, Zheng C, Peng Z, Zhao H, Lang J, Liang L, et al. Theoretical study of microcavity-enhanced absorption spectroscopy for mid-infrared methane detection using a chalcogenide/silica-on-fluoride horizontal slot waveguide racetrack resonator. Opt Express 2020;28:21432–46.